NORTHWESTERN UNIVERSITY

Magnetoelectric cobalt ferrite/bismuth ferrite hybrid nanostructures: Progress towards achieving electric field control of magnetization

SENIOR HONORS THESIS

Field of Physics

By

Alexandra R. Cunliffe

Advisor: Professor Venkat Chandrasekhar

EVANSTON, ILLINOIS

May 2009

ABSTRACT

Developments towards a magnetoelectric composite material, cobalt ferrite/bismuth ferrite are presented. In this experiment, electron beam lithography and a chemical sol gel precursor deposition method were employed to form arrays of $CoFe_2O_4$ nanopillars on SiO_2 and ferroelectric $BiFeO_3$ substrates. Tests including atomic force and magnetic force microscopy, x-ray diffraction, SQUID magnetometry, and ferromagnetic resonance spectroscopy were carried out on the samples. Results showed that $CoFe_2O_4$ nanostructures with interesting magnetic and topographical properties had formed. Atomic force microscope imaging of $CoFe_2O_4$ on both SiO_2 and $BiFeO_3$ substrates shows significant structural differences: While the structures grown on SiO_2 are uniform in shape and size, nanopillars grown on $BiFeO_3$ follow the substrate's rough surface topography, resulting in irregular nanostructures. Furthermore, overgrowth beyond PMMA thickness for the $BiFeO_3$ nanopillars suggests that faceted $CoFe_2O_4$ may have formed on this substrate. Magnetic data obtained from both SQUID magnetometry and ferromagnetic resonance spectroscopy shows that the nanopillars fabricated on SiO_2 are polycrystalline with multiple magnetic domains, indicating that even at this small length scale, magnetocrystalline anisotropy dominates over shape anisotropy.

CHAPTER 1

Motivation

Since the discovery of multiferroics, these materials have generated a great deal of interest both because of their magnetic and electric properties and their potential for application in electronic devices [**1, 2**]. The coupling between the electric polarization and intrinsic magnetization of these materials allows for the observation of the magnetoelectric effect: An applied external electric field causes the magnetic dipoles to reorient, resulting in a net shift in the materials magnetization direction. Such magnetic control would allow for magnetic switching using an applied electric field, an effect which could be applied towards improving memory devices and electronic systems.

Naturally-occurring multiferroics such as Cr_2O_3, Ti_2O_3, $GaFeO_3$, $PbFe_{0.5}Nb_{0.5}O_3$, and numerous others have been widely investigated [**3, 4, 5, 6**]. Although these materials exhibit the magnetoelectric effect, the changes are not significant enough to allow for large-scale applications [**7**]. Recently, there has been growing interest in the fabrication of synthetic multiferroics. Artificial synthesis of magnetoelectric devices promises to solve the problem of weak magnetoelectric coupling that exists in naturally-occurring multiferroics, since the intrinsic electric and magnetic properties of the ferroelectric and ferromagnetic components allows for a measurable shift in the internal magnetization of the material when an external electric field is applied. Several groups have already attempted to fabricate composite ferroelectric/ferromagnetic nanostructures [**8**]. In most cases, however, the proposed methods involve chemical etching or ion-beam milling. These

procedures damage the substrate, oftentimes rendering it conductive and hindering its magnetoelectric capabilities.

A procedure to fabricate multiferroic devices composed of ferroelectric bismuth ferrite ($BiFeO_3$) and ferrimagnetic cobalt ferrite ($CoFe_2O_4$) is presented. Both materials have Curie temperatures that are far above room temperature and maintain their ferroelectric and ferromagnetic properties on the nanometer length scale. In this regard, they are already significantly better than naturally-occurring multiferroics, which have substantially lower Curie temperatures, and elemental magnetic materials, which in many cases become superparamagnetic on a small length scale. Here electron beam lithography and a chemical sol-gel precursor deposition method are employed to form arrays of $CoFe_2O_4$ nanopillars on SiO_2 and ferroelectric $BiFeO_3$ [**9, 10**]. $CoFe_2O_4$ sol-gel is deposited by spinning onto a substrate that has been patterned using electron beam lithography. The mask is removed following a standard lift-off procedure, and the wafer is annealed for several hours. Lattice matching between the resulting arrays of $CoFe_2O_4$ nanopillars and $BiFeO_3$ substrate is expected to allow for growth of single domain $CoFe_2O_4$ on the $BiFeO_3$ [**11**]. Such $CoFe_2O_4$ crystal growth on $BiFeO_3$ would achieve the goal of multiferroic material synthesis, giving rise to a system with novel magnetoelectric properties.

CHAPTER 2

Background

2.1. The Magnetoelectric Effect

The magnetoelectric effect comes about as natural result of the interplay between a material's electric polarization and an external magnetic field, or conversely, between the material's intrinsic magnetization and an external electric field. In the case of an electrically-polarized magnetoelectric, an applied *magnetic* field causes the *electric* dipoles that make up the material to be altered, and once the magnetic field is removed, the electric polarity of the material does not revert back to its original state. The same is true for a magnetoelectric with an intrinsic magnetization: An applied *electric* field causes the *magnetic* dipoles of the material to change direction. Once the electric field is removed, the magnetic dipoles do not revert to their original state, resulting in the permanent transformation of the magnetization direction of the material. In the first case, this phenomenon is referred to as the direct magnetoelectric effect while, for the case of a magnetic material in an electric field, it is called the converse magnetoelectric effect.

The existence of the magnetoelectric effect was first hypothesized in the late eighteenth and early nineteenth centuries by scientists who noted, independently of one another, the effect that a magnetic field had on the electric polarization of a dielectric and the effect of an electric field on the magnetization of a dielectric [**12, 13**]. Recently, interest

in the magnetoelectric effect has been revived because of the implications that electric control of magnetization would have in the electronics industry. Materials that exhibit the magnetoelectric effect could be used, for example, towards more efficient memory devices and spin-based electronics, such as improved generators, transformers, and magnetic field sensors [**20**].

A materials magnetoelectric properties can be explicitly represented by considering the equations that govern the electric polarization (P) and magnetization (M) of the material. These values are found by differentiating the material's Helmholtz free energy (F) [**7, 14**]:

$$P = -\delta F/\delta E = \kappa_{ij} E_j + \alpha_{ij} H_j \tag{2.1}$$

$$M = -\delta F/\delta H = \chi_{ji} H_j + \alpha_{ji} E_j \tag{2.2}$$

where H and E are the magnetic and electric fields respectively. κ_{ij} and χ_{ji} are constant tensors dependent on the electric susceptibility ϵ and magnetic susceptibility μ of the material. α_{ij} is called the magnetoelectric susceptibility tensor. It denotes the strength of the coupling between electric and magnetic effects, i.e., the amount of electric polarization induced by a magnetic field or the amount of magnetization induced by an electric field. If α_{ij} is significantly large, changes in magnetic field H will effect the value of the electric polarization P and, likewise, changes in the electric field E will adjust the value of the magnetization M.

In order to fully comprehend the magnetoelectric effect, we must first consider individually the properties that allow for the magnetoelectric effect to be observed in a material. In the following sections, I will discuss two types of polarized materials called ferroelectrics and ferrimagnets. I will then examine the magnetoelectric properties exhibited by composites called multiferroics.

2.2. Ferroelectricity and Ferroelectrics

A material is said to be ferroelectric when it exhibits an intrinsic electric polarization in the absence of an electric field. Such polarization can be clearly illustrated by looking at the crystal lattice structure of certain types of ferroelectric materials. For example, the ferroelectric effect is often observed in the case of materials having a perovskite lattice structure [**15**]. This crystal structure is depicted in Figs. 2.1(a) and 2.1(b). The atoms represented by blue and orange spheres are generally positively-charged cations. The red atoms are most commonly oxygen ions with a negative charge. The negatively charged oxygen ions exert an electrostatic force on the positive cations, causing distortion of the crystal structure (Fig. 2.1(c)). The arrows depict the stretching motion due to the electrostatic force. The result is the electrically polarized material shown in Fig. 2.1(d).

The ferroelectricity of a material also depends on temperature. Above a certain temperature, called the ferroelectric Curie temperature, the polarized structure of the crystal lattice becomes energetically unfavorable, and a transition from a ferroelectric to non-ferroelectric state occurs. In the case of a common ferroelectric, $BaTiO_3$, the Curie temperature T_c is 135° C [**15**]. For $BiFe_3O_4$, the ferroelectric used in this experiment, the Curie temperature is significantly higher, roughly 400° C.

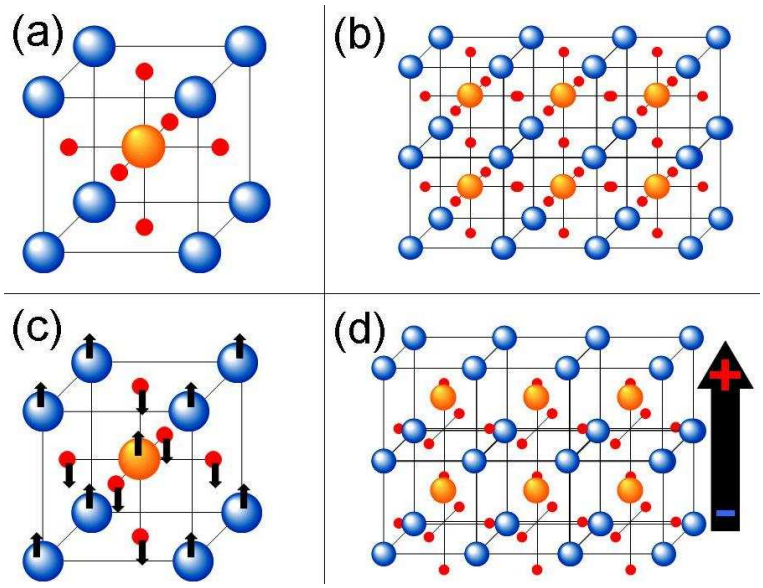

Figure 2.1. Schematic of the ferroelectric effect for a perovskite. (a) A perovskite unit cell. (b) A perovskite lattice. (c) Crystal structure distortion due to electrostatic forces between the ions. (d) Resulting electric polarization of the crystal.

In some cases, external conditions lead certain materials to exhibit spontaneous polarization. For example, pyroelectrics such as $PbTiO_3$ will gain internal electric dipole moments when the material is subjected to heat. As temperature rises, the dielectric constant of the material gradually increases until, at a critical temperature, it reaches a maximum. Beyond this temperature, the material is no longer ferroelectric because the temperature exceeds the Curie temperature of the material [**15**]. All ferroelectrics exhibit electric polarization when the material is subjected to stress or strain. This is called the piezoelectric effect.

2.3. Piezoelectric Effect

The piezoelectric effect is a phenomenon whereby mechanical stress or strain leads to reorientation of electric dipoles through a material, inducing a spontaneous change in the charge polarization. All ferroelectrics exhibit the piezoelectric effect (although all piezoelectrics are not necessarily ferroelectric). The piezoelectric effect may be formally described by the following set of equations, which provide a relationship between the electric displacement D, the electric field E, and the stress and strain, T and S respectively [**16**]:

$$D = \epsilon_T E + d_{33} T \tag{2.3}$$

$$S = d_{33} E + s_E T \tag{2.4}$$

where ϵ_T is the dielectric constant and d_{33} is the piezoelectric constant. s_E is the material's compliance in the presence of a constant electric field. This constant describes the stress-strain relationship for a material and is based on the material's Young's modulus and Poisson's ratio [**17**]. From the equations above, it can be seen that any increase or decrease in stress (T) or strain (S) on the material will lead to an increase or decrease in electric displacement (D) and in the material's electric field (E). These relations also predict the existence of the converse piezoelectric effect, whereby a piezoelectric material physically changes shape when an external electric field E is introduced. This altered shape is a result of an increase in stress T and strain S on the material due to the electric

field change. The piezoelectric effect is used in a variety of applications because the crystal motion resulting from the electric field is both predictable and precise. Common piezoelectrics include Lead-Zirconate-Titanate (PZT) and bismuth ferrite [**16**]. Figures 2.2(a) and 2.2(b) provide a schematic representation of the piezoelectric effect. The blue circles in the figure denote positively-charged ions while the pink circles denote negatively-charged ions. Due to its lattice structure, the material has an intrinsic polarization P_o in its initial state (Fig. 2.2(a)). In Fig. 2.2(b), the material is subject to mechanical stress. The charge distribution within the material is altered, leading to a new polarization P_f:

$$P_f = P_o + \Delta P \tag{2.5}$$

Figures 2.2(c) and 2.2(d) demonstrate the converse piezoelectric effect. The external electric field represented by green arrows leads the ions in the material to shift: the positively-charged ions move in the positive z-direction while the negatively-charged ions move in the opposite direction. The result is a distortion of the physical shape of the piezocrystal:

$$x_f, y_f, z_f = x_o, y_o, z_o + \Delta x, \Delta y, \Delta z \tag{2.6}$$

As noted before, a material need not be ferroelectric in order to demonstrate the piezoelectric effect. The dipole moments of a material may be in equilibrium until stress or strain disrupts this equilibrium, leading to non-zero electric polarization. Such is the case for the common piezoelectric quartz. While this is an interesting phenomenon, it will not be discussed in great detail here, as $BiFeO_3$ is a ferroelectric piezoelectric. It

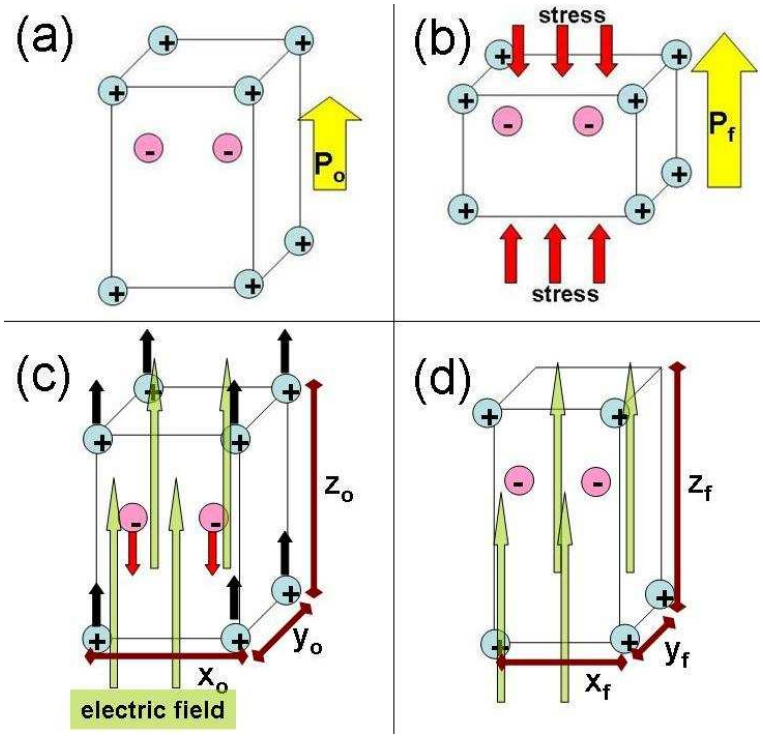

Figure 2.2. A schematic of the piezoelectric effect ((a) and (b)) and the inverse piezoelectric effect ((c) and (d)). (a) Intrinsic electric polarization of the material prior to applied stress. (b) Applied stress causes the electric polarization strength to change. (c) An external electric field is applied to a piezoelectric, causing the ions to shift. (d) The shape of the crystal is altered due to the movement of ions.

is also worth noting that, as is the case for all ferroelectrics, the piezoelectric effect can only be observed for materials below the ferroelectric Curie temperature since above this temperature, the net electric polarization is zero.

2.4. Ferromagnetism and Ferromagnetic Materials

We now shift from the domain of electric polarization and ferroelectricity to the subject of ferromagnetism and the ferromagnetic properties of certain materials. Here I will discuss materials in which polarized magnetic dipole moments lead a material to show

a net magnetization. The most well-known material that exhibits magnetic properties is the ferromagnet. For a ferromagnet, all magnetic dipoles in a domain are in parallel alignment. Even if all magnetic dipoles are not aligned, however, a net magnetic moment may still be observed. Such is the case with a ferrimagnet, a material in which the sum of the magnetic dipole moments in one direction is stronger than the net magnetic moment in the antiparallel direction. The magnetic dipole orientations for both a ferromagnet and a ferrimagnet are depicted in Fig. 2.3.

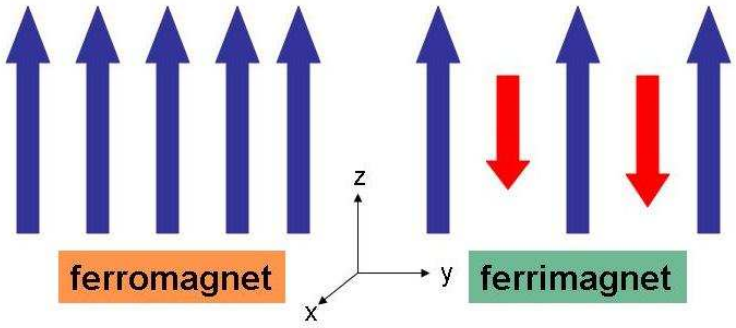

Figure 2.3. Magnetic dipole alignment for a ferromagnet and a ferrimagnet.

The magnetic dipole alignment of a ferrimagnet is a result of the material's crystal structure, which requires magnetic ions in the crystal lattice to assume an antiparallel spin configuration. This effect can be seen more clearly by considering the common ferrimagnet magnetite ($Fe^{3+}(Fe^{2+}Fe^{3+})O_4$), which has a perovskite crystal structure like that of $CoFe_2O_4$. The crystal lattice and ion spin orientation of magnetite is shown in Fig. 2.4(a). The iron ions are positively charged($Fe^{3+}, Fe^{3+}, Fe^{2+}$) while the oxygen ions have negative charge (O^{2-}). The close proximity of the Fe^{3+} ions to one another leads the orbitals to overlap. Pauli exclusion principle restricts the electrons from residing in the same spin state, and so the electrons assume an antiparallel alignment. Meanwhile, the Fe^{3+}

and Fe^{2+} ions will maintain parallel spins due to a "double exchange" interaction that occurs between the two ions. Through this interaction, an electron effectively "jumps" from Fe^{3+} to O^{2-}, resulting in Fe^{2+}. At the same time another electron "jumps" from O^{2-} to Fe^{2+}, resulting in Fe^{3+}. This double exchange interaction is depicted in 2.4(b). In order for exchange to occur, parallel spin configuration is required. The net magnetic moment of this material points upwards simply because more ion spins (and thus magnetic moments) are oriented in the upward direction [**18**].

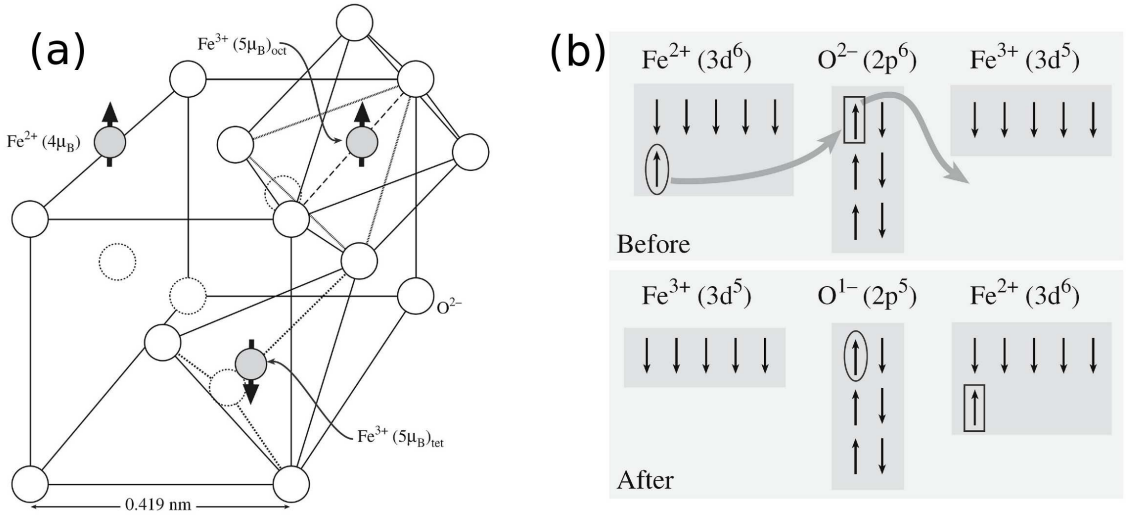

Figure 2.4. Ferrimagnetism exhibited by magnetite. (a) The orientation of the ion spins in the crystal lattice. (b) An illustration of the double exchange interaction which leads Fe^{3+} and Fe^{2+} to have parallel spin configuration. Images taken from [**18**].

Magnetic materials, like ferroelectrics, exhibit magnetic properties only up to a certain point, also called the Curie temperature. Above this critical temperature, the magnetic dipoles are reoriented from an ordered to a random fashion, resulting in no net magnetization. In the case of ferrimagnetic $CoFe_2O_4$, the Curie temperature is far above room temperature, allowing for its use in this experiment.

2.5. Magnetostrictive Materials

Not surprisingly, there exists a magnetic parallel to a piezoelectric, referred to as a magnetostrictive material. For a piezoelectric, reorientation of the material's net electric polarization causes the structure to physically change shape. Equivalently, when a magnetostrictive material is subject to an external magnetic field, the magnetic field alters the shape of the material. Practically all ferromagnets (and ferrimagnets) are magnetostrictives. At room temperature, cobalt is the most magnetostrictive pure element [**19**].

A magnetostrictive material alters its shape as a result of two phenomena. First, the magnetic dipoles spin about their axis in order to reorient to match the external magnetic field. Second, the force felt by the external field causes the domain walls to migrate. These changes that occur on the level of individual dipoles and on the scale of domain walls both contribute to the shape change [**19**].

2.6. Multiferroics

Materials that exhibit both ferroelectric and ferromagnetic properties are referred to as multiferroics. As stated previously, examples of naturally-occuring multiferroics include Cr_2O_3, Ti_2O_3, $GaFeO_3$, and $PbFe_{0.5}Nb_{0.5}O_3$ [**3, 4, 5, 6**]. A multiferroic exhibits the magnetoelectric effect due to the interplay between its piezoelectric and magnetostrictive properties. Under the influence of an applied magnetic field, its shape is altered because the material is magnetostrictive. The changing shape subjects the material to stress or strain. Because the material is also piezoelectric, the stress or strain induces a spontaneous change in net electric polarization. Conversely, when the material is brought into an

external electric field, it changes shape because of its piezoelectric properties. This altered shape leads to a net magnetization because of the magnetostrictive properties of the material. To summarize, we have, in the case of a multiferroic, a material in which an applied *magnetic* field alters the *electric* polarization or an applied *electric* field alters the *magnetization*.

2.7. Fabrication of Composite Materials

If magnetization could be easily and efficiently controlled by the application of an electric field, the implications would be great for the electronics industry [**20**]. However, complications arise when trying to use naturally-occuring multiferroics for this purpose. Many multiferroics have a Curie temperature that is below room temperature, resulting in a loss of ferroelectricity or ferromagnetism when the materials are used in an ambient environment. As of yet, all known multiferroics with a Curie temperature above room temperature exhibit ferromagnetic/ferroelectric coupling that is too weak to contribute to large-scale magnetic switching [**7**]. In order for the magnetoelectric effect to be applied for industrial use, it is necessary to fabricate multiferroic composites with pronounced ferroelectric and ferromagnetic properties.

Manufactured composites have the potential to allow for far more efficient applications of magnetic switching than naturally-occuring multiferroics. The use of individual ferroelectrics and ferrimagnets is more practical because there are many materials for which the Curie temperature is significantly above room temperature. Additionally, the strength of a multiferroic is dependent on the individual strength of the ferroelectric and magnetic

components. A material that is strongly ferroelectric exhibits a large change in polarization in the presence of an external electric field and will change shape noticeably due to its piezoelectric properties. Likewise, a material with strong ferromagnetic properties experiences a significant change in net magnetization in the presence of a magnetic field, and due to its magnetostrictive properties, it will experience a change in magnetization when its shape is altered by an external force. Figure 2.5 illustrates how the coupling between a ferroelectric (Fig. 2.5(a)) and a ferrimagnet (Fig. 2.5(b)) could lead to the observation of a significant magnetoelectric effect. In Fig. 2.5(c), an applied electric field has successfully altered the magnetization direction of the composite ferroelectric/ferromagnetic material.

This relationship can be seen mathematically by once again considering the equations governing the electric polarization P and magnetization M of a magnetoelectric:

$$P = \kappa_{ij} E_j + \alpha_{ij} H_j \tag{2.7}$$

$$M = \chi_{ji} H_j + \alpha_{ji} E_j \tag{2.8}$$

The magnetoelectric susceptibility tensor, α_{ij}, is limited by the electric and magnetic susceptibilities (ϵ and μ respectively) of the material [**7**]:

$$\alpha_{ij}^2 < \epsilon\mu \tag{2.9}$$

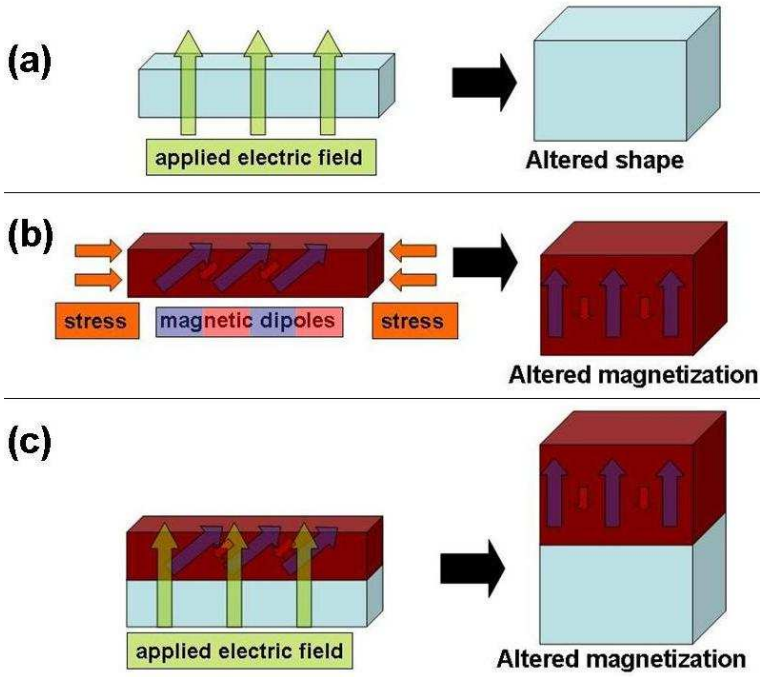

Figure 2.5. The magnetoelectric effect for a composite material. (a) An applied electric field causes a ferroelectric to change shape. (b) Mechanical stress alters the magnetic dipole moment of a ferrimagnet. (c) A composite ferroelectric/ferrimagnetic material experiences an altered magnetization resulting from an applied electric field.

so a composite material, which has large ϵ due to the ferroelectric component and large μ due to the ferrimagnetic component, will allow for larger magnetoelectric susceptibility α_{ij}.

CHAPTER 3

Experiment

3.1. Experimental Overview

This experiment aims to develop a composite material for which the magnetoelectric effect is pronounced. A combination of electron beam lithography and a sol-gel based chemical route were employed to fabricate ferrimagnetic cobalt ferrite ($CoFe_2O_4$) nanopillars on oxidized silicon and ferroelectric bismuth ferrite ($BiFeO_3$). Cobalt ferrite was chosen both because of its ferrimagnetic properties and inverse spinel structure, which allows for lattice matching between the $CoFe_2O_4$ and $BiFeO_3$ and results in epitaxial growth of the $CoFe_2O_4$ on $BiFeO_3$. The composite $CoFe_2O_4/BiFeO_3$ system is therefore an ideal multiferroic with properties that can be exploited to allow for magnetic orientation control.

Prior to the fabrication of multiferroic $CoFe_2O_4/BiFeO_3$, several other experiments were carried out to ensure optimal results. First, a thin film of the sol-gel precursor was grown on a SiO_2 wafer to probe the magnetic properties of the material formed using the sol-gel method. $CoFe_2O_4$ nanopillars were then fabricated using a patterned SiO_2 wafer. SiO_2 is far more durable than $BiFeO_3$, and so by using this substrate, isolated tests were easily performed to determine the success of $CoFe_2O_4$ nanopillar fabrication. Once the integrity of both the sol-gel precursor and the experimental methods had been established,

$CoFe_2O_4$ nanopillars were fabricated on $BiFeO_3$ using the following procedure: The sol-gel precursor was deposited on the patterned PMMA/$BiFeO_3$ substrate through spinning. The wafer was then baked for several minutes to gelate the solvent. After liftoff of the PMMA mask had been achieved, the substrate was annealed for five hours, allowing the aqueous sol to evaporate and resulting in arrays of hard metallic $CoFe_2O_4$ nanopillars. For oxidized silicon, the annealing was performed in air, while for $BiFeO_3$, the substrate was annealed in the presence of bismuth powder so as to compensate for any potential loss in bismuth. A flow chart of the experimental procedure is show in Fig. 3.1.

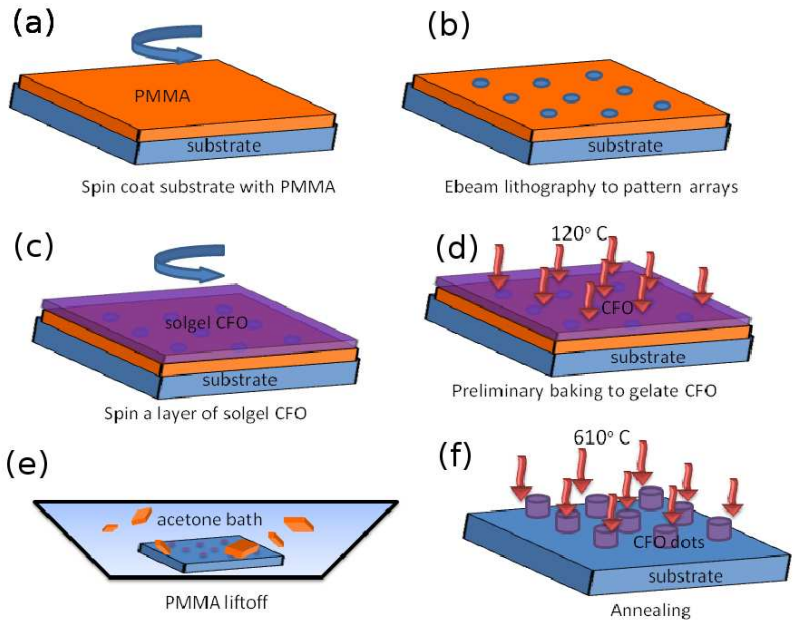

Figure 3.1. Schematic representation of the procedure used to fabricate arrays of $CoFe_2O_4$ on a substrate. (a) The substrate is spin-coated with PMMA. (b) An array of elliptical dots is patterned on the PMMA using electron beam lithography. (c) The sample is spin-coated with a layer of $CoFe_2O_4$ sol precursor. (d) The sample is baked initially at 120° C for five minutes to gelate the sol. (e) The PMMA is lifted off using acetone. (f) The sample is annealed at 610° C for five hours.

Throughout the experiment, a variety of tests were carried out to probe the topographical and magnetic composition of the material. These tests include atomic force microscopy, magnetic force microscopy, ferromagnetic resonance imaging, X-ray diffraction, and SQUID magnetometry. These results are discussed in greater detail in subsequent portions of the paper.

3.2. Preparation of Sol-gel Precursor

To prepare the sol-gel precursor to $CoFe_2O_4$, a standard procedure was followed in which powders of cobalt and iron compounds were dissolved in an alcohol-based solvent [**21**]. First, 1 g of 2-methoxyethanol was added to 30 mL of diethanolamine, and the solution was stirred until the components were fully combined. 74.7 mg (1/200 mol) of cobalt acetate powder ($Co(CH_2CO_2)_2 \cdot 4\,H_2O$) and 242.4 mg (1/100 mol) of iron nitrite powder ($Fe(NO_3)_3$) were added to the aqueous solution. The solution was stirred for several minutes until the powders were completely dissolved in the liquid. The container was then placed in a water bath and refluxed at 70° C for 4 hours. The experimental setup is shown in Fig. 3.2(a). Reflux was done using a Liebig condenser, a tube composed of two concentric cylinders that was attached to the flask containing the sol-gel precursor. As the solution was heated, water vapor rose into the internal cylinder and was immediately cooled by water flowing through the outside cylinder. In this way, the solution was prevented from evaporating during heating. The prepared $CoFe_2O_4$ sol-gel precursor is shown in Fig. 3.2(b). Following preparation, the solution was immediately ready for use.

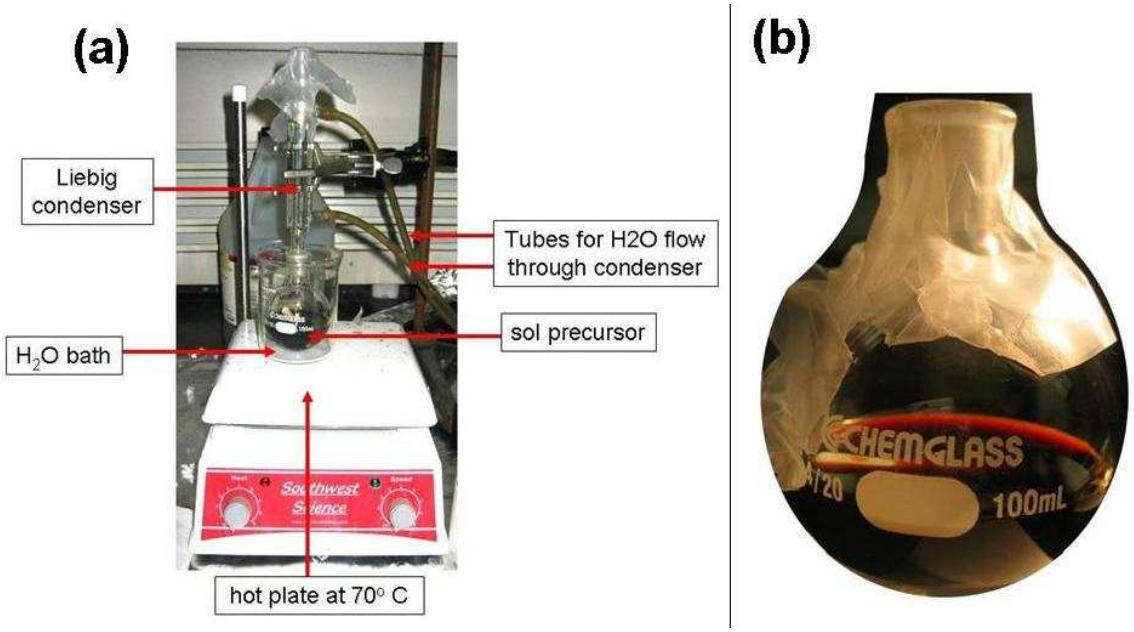

Figure 3.2. (a) Experimental set-up for the preparation of the $CoFe_2O_4$ sol precursor. (b) The prepared $CoFe_2O_4$ sol precursor.

3.3. Fabrication and Analysis of $CoFe_2O_4$ thin films

To better characterize the physical properties of the material synthesized by the sol-gel method, a thin film of the sol-gel precursor was deposited on a SiO_2 substrate. The wafer was spin-coated with the precursor then baked at 120° C to gelate the solution. It was then annealed in atmosphere at 610° C for 5 hours. A number of wafers were prepared in this fashion in order to determine the optimal deposition and spinning parameters. The spin speeds ranged from 500 to 4000 rpm and the spin time ranged from 30 to 60 seconds. Prior to spinning, several of the wafers were etched with oxygen plasma at 60 W for 30 s using a plasma etching device that had been fabricated in-house. During the etching process, a 100 mT vacuum pressure was maintained. Visual indications suggested a successful deposition: $CoFe_2O_4$ of reasonable thickness and smoothness showed up as a

blue-green film on the purple SiO_2 wafer. Color variation (anywhere from blue to green to yellow) depended on the thickness of the $CoFe_2O_4$ film. Unsuccessful depositions were marked either by obvious granularity of the $CoFe_2O_4$, or no change in the color of the wafer, indicating that $CoFe_2O_4$ failed to accumulate on the substrate. Fig. 3.3(a) shows an oxidized silicon wafer prior to sol deposition, and Figs. 3.3(b) and 3.3(c) show two wafers synthesized using the method described above. The granularity of the wafer of Fig. 3.3(b) was due to the slow spinning speed (1000 rpm). The wafer of Fig. 3.3(c) was synthesized by first etching the SiO_2 wafer with oxygen plasma then spin-coating the sol onto the wafer at 1500 rpm for 30 s. The parameters used in this case appeared optimal, and further tests were carried out to better characterize the physical properties of the thin film of Fig. 3.3(c).

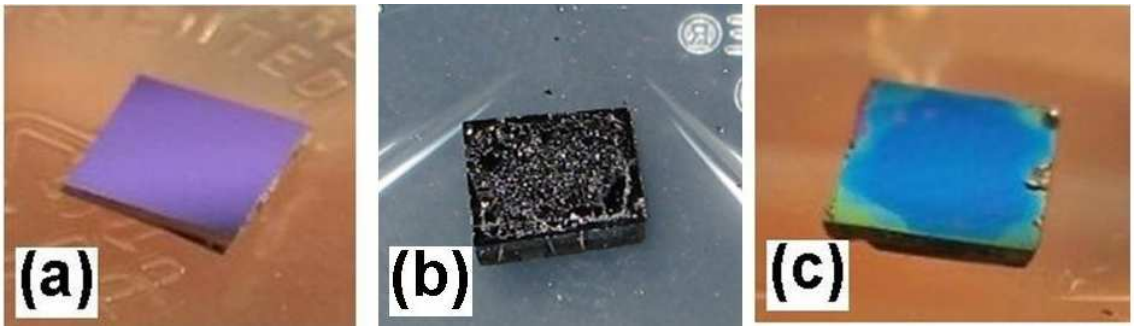

Figure 3.3. Samples obtained from the deposition of the $CoFe_2O_4$ sol precursor on SiO_2 wafers. (a) A SiO_2 wafer prior to deposition. (b) Unsuccessful deposition of the $CoFe_2O_4$ sol precursor is indicated by the granular structures on the wafer. (c) Successful deposition of the $CoFe_2O_4$ sol precursor is suggested by the blue-green film present on the wafer.

3.3.1. X-ray Diffraction

In order to determine the nature of the material formed by the synthesis procedure outlined above, grazing incidence x-ray diffraction (XRD) was performed on a thin film of the sol gel deposited on oxidized silicon. XRD was carried out at the J.B. Cohen X-ray Diffraction Facility at Northwestern University. If the thin film has a crystal structure identical to the structure of $CoFe_2O_4$, peak intensities should be observed at the locations of the $CoFe_2O_4$ Miller indices. Figure 3.4 shows the spectrum obtained when XRD was performed. Above each peak on the intensity curve, the corresponding $CoFe_2O_4$ Miller index is listed. This test confirms that the material formed using the sol gel method is polycrystalline $CoFe_2O_4$.

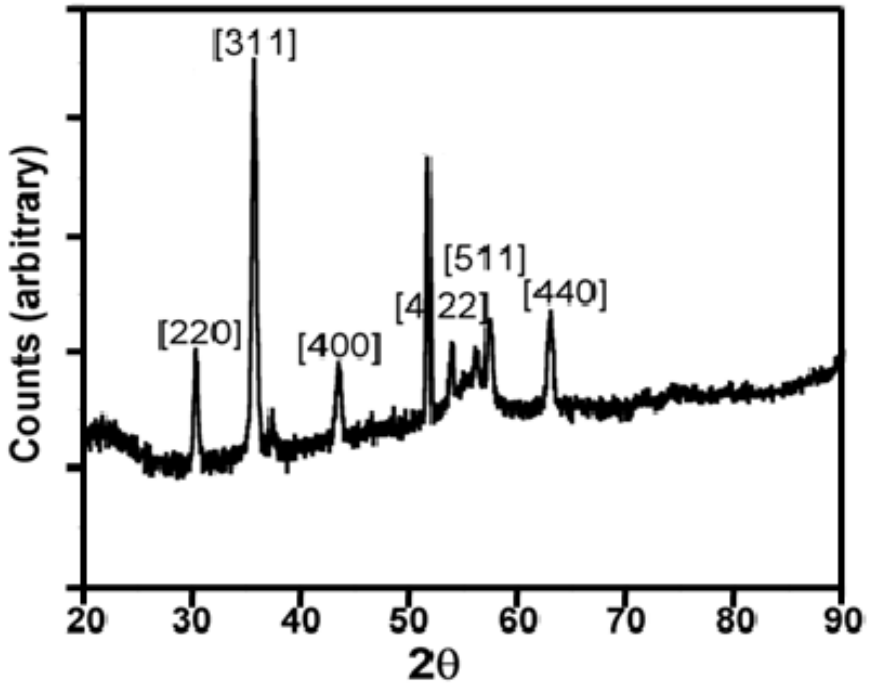

Figure 3.4. X-ray diffraction of the thin film. Each intensity peak is labeled with the corresponding $CoFe_2O_4$ Miller index.

3.3.2. Atomic Force Microscopy / Magnetic Force Microscopy

To further probe the topographical and magnetic properties of the thin film, it was imaged using both atomic force microscopy (AFM) and magnetic force microscopy (MFM) in a TESCAN atomic force microscope. AFM imaging (Fig. 3.5(a)) reveals that the surface of the film is granular with average surface roughness of 2 nm. The MFM image shown in Fig. 3.5(b) indicates large domains (∼200 nm) that show up as areas of light and dark contrast. These results suggest that multiple domains of magnetic $CoFe_2O_4$ were formed. Furthermore, this indicates that on the length scale of roughly 200 nm, it may be possible to observe single magnetic domains of $CoFe_2O_4$.

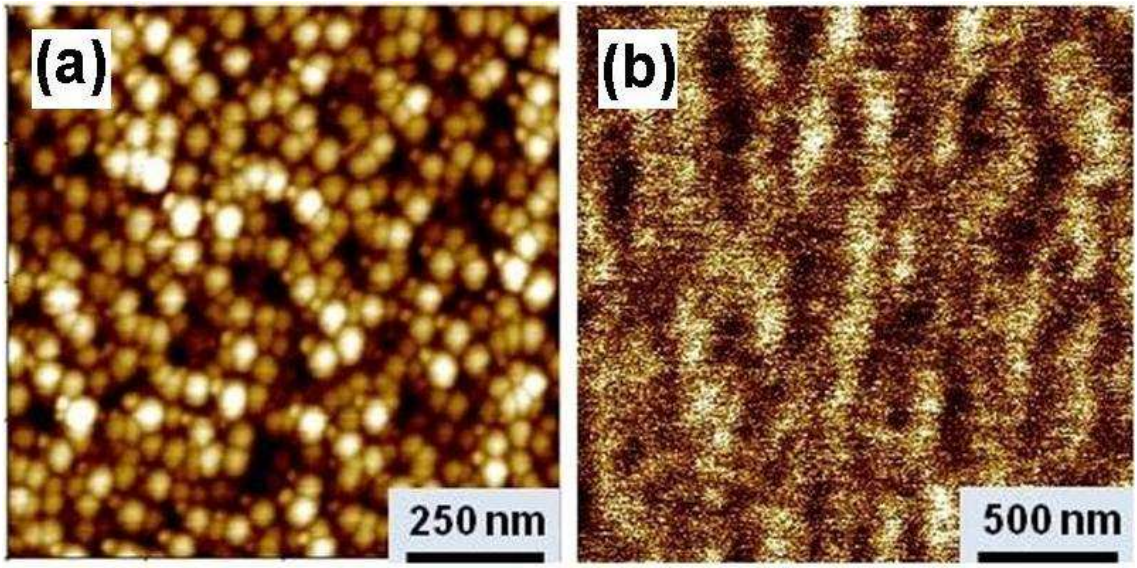

Figure 3.5. Atomic force microscopy(AFM) and magnetic force microscopy(MFM) of the thin film. (a) The AFM image shows that the surface is granular with average surface roughness of 2 nm. (b) The MFM image shows the presence of 200 nm magnetic domains represented by areas of light and dark contrast.

3.3.3. Scanning Electron Microscopy

In addition to atomic force microscopy, scanning electron microscopy of the thin film was carried out to further characterize the topographical properties of the material. Figure 3.6 reveals that the grains deposited on the SiO_2 are crystalline, indicating that a polycrystalline thin film has been successfully grown. Furthermore, the crystalline shape is characteristic of materials that are inverse spinel, which is the crystal structure of $CoFe_2O_4$.

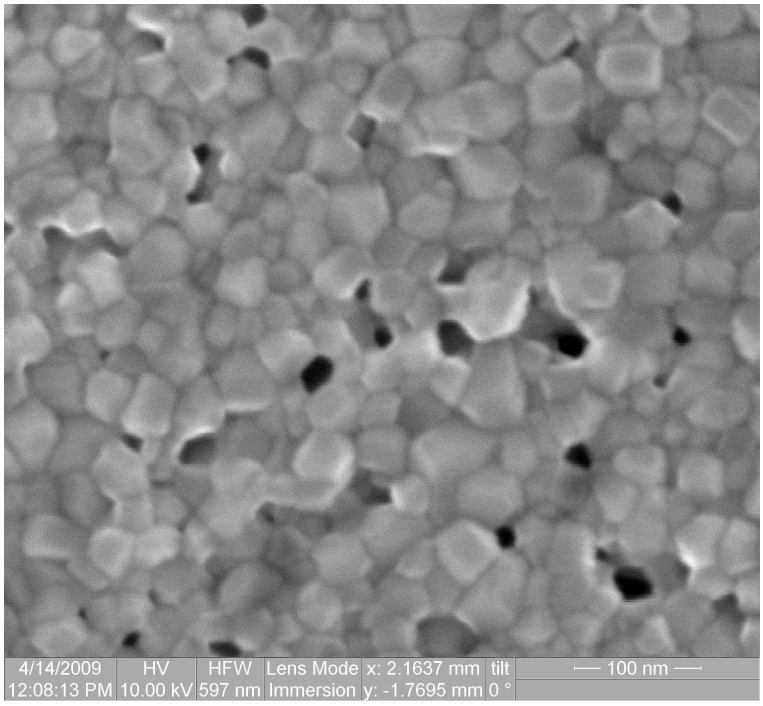

Figure 3.6. Scanning electron microscopy of the film. The shape of the crystals suggests that the material is inverse spinel, which is the lattice structure of $CoFe_2O_4$.

3.3.4. SQUID Magnetometry

A Quantum Design MPMS Superconductiong Quantum Interference Device (SQUID) magnetometer was used to measure the magnetization (M) of the film as a function of the applied magnetic field (H). The magnetic field was ramped first from negative to positive, then from positive to negative. If the material was single-crystalline, the magnetic dipole reorientation would result in abrupt changes in magnetization, indicated by sharp lines in the hysteresis loop. In Fig. 3.7, however, a smooth hysteresis loop is observed, indicating that the material is polycrystalline and consists of multiple magnetic domains. Furthermore the material's coercive field, the field required to reduce the magnetization from saturation to zero, is 500 Oe, which is much larger than the coercive field for ferromagnets like cobalt (coercive field $\approx$ 15 Oe) or permalloy (coercive field $\approx$ 90 Oe) [**22, 23**]. This suggests that, unlike elemental ferromagnets, the material is a hard ferromagnet that will not become superparamagnetic at the nanometer length scale.

3.4. Electron Beam Lithography

Electron beam lithography was employed to write arrays of elliptical dots on a layer of polymethyl methacrylate (PMMA) that had been deposited on the SiO_2 and $BiFeO_3$ substrates. Prior to writing, the substrate was first sonicated for several minutes in acetone and isopropyl alcohol to clean the surface. The PMMA mask was then deposited on the substrate by spinning at 4000 rpm for 60 seconds. The wafer was baked at 170° C for 30 minutes. Arrays of elliptical dots covering a total surface area of 1 mm^2 were patterned on the PMMA using electron beam lithography. The dots were made elliptical so as to introduce shape anisotropy in the $CoFe_2O_4$ pillars. This anisotropy is expected

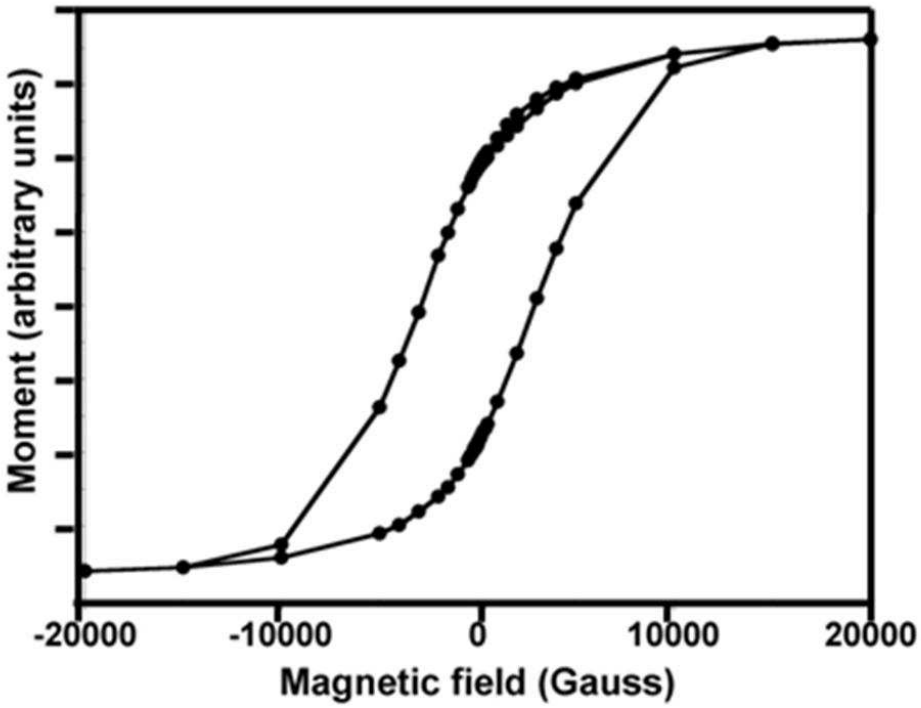

Figure 3.7. The hysteresis loop of the thin film obtained using SQUID magnetometry. The coercive field of the film is 500 Oe, indicating that the material is a hard ferromagnet. Furthermore, the curved shape of the hysteresis loop shows that material is polycrystalline. This test was carried out by Dr. Goutam Sheet.

to cause the magnetic dipoles of the $CoFe_2O_4$ dots to orient in the same direction (along the major axes) during annealing. The major axes of the elliptical dots were 300 nm long and the minor axes were 200 nm long. To pattern the array on SiO_2, the voltage of the electron beam was 30 kV, the beam current was 10 pA, and the dosage of the PMMA was 300 $\mu C/cm^2$. For the array on $BiFeO_3$, the beam voltage was 10 kV, the beam current was 8 pA, and the dosage was 120 $\mu C/cm^2$. The parameters were adjusted for $BiFeO_3$ because it is an insulating material, unlike SiO_2 which is highly conductive. Therefore, a lower voltage is necessary to prevent the material from charging, which could deflect

the electron beam during writing. After the writing procedure was complete, a methyl isobutyl ketone (MIBK) and isopropyl alcohol (IPA) solution was used as the developer. MIBK:IPA were combined in a 1:3 ratio, and the solution was heated to 24° C. A stream of the MIBK/IPA was then allowed to run over the wafer for 60 s. Dark field optical microscopy verified that arrays of dots had been successfully written on the PMMA.

3.5. $CoFe_2O_4$ nanopillars on SiO_2

The magnetic and topographical imaging outlined in the previous section provide strong evidence that the sol-gel precursor yields polycrystalline $CoFe_2O_4$ when the solution is deposited onto SiO_2 wafers and proper preparation methods are followed. The next step is to attempt to fabricate pillars of magnetic $CoFe_2O_4$ on SiO_2 substrate.

3.5.1. Nanopillar fabrication procedure

To prepare the $CoFe_2O_4$ pillars on SiO_2, the sol-gel precursor was spin-coated onto the patterned substrate. The substrate was patterned using the procedure outlined earlier (see 3.4 Electron Beam Lithography), and the spinning parameters were the parameters that had been determined earlier to yielded optimal results when preparing the thin film of $CoFe_2O_4$ on SiO_2 (1500 rpm for 30s; see 3.3 Fabrication and Analysis of $CoFe_2O_4$ thin films). Following spinning, the wafer was baked for 5 minutes at 120° C in order to gelate the solution. Then, lift-off was accomplished by submerging the wafer in a warm acetone bath for several minutes. Once the PMMA had been successfully removed, leaving behind only pillars of metallic material on the SiO_2, the wafer was annealed in atmosphere for five hours at 610° C.

3.5.2. Analysis of nanostructures

Once the nano-pillars had been successfully fabricated on the SiO_2 substrate, various imaging methods were employed to fully characterize the magnetic and topographical properties of the material. Dark field optical imaging (Fig. 3.8(a)) reveals that metallic dots have formed in a regular array on the substrate. The spacing between the dots is 5 microns, which ensures minimal magnetic interaction between two adjacent nano-pillars. Figures 3.8(b) and 3.8(c) show additional images of the nanostructure array, this time obtained through scanning electron microscopy. These images confirm the optical data of Fig. 3.8(a) and provide detailed information about the topography of the nanostructures. From Fig. 3.8(c), we see that the pillars are smooth with a height of less than 100 nm. The dots show no apparent crystal structure, which is to be expected because the lattice structures of $CoFe_2O_4$ and SiO_2 are dissimilar, hindering crystalline growth.

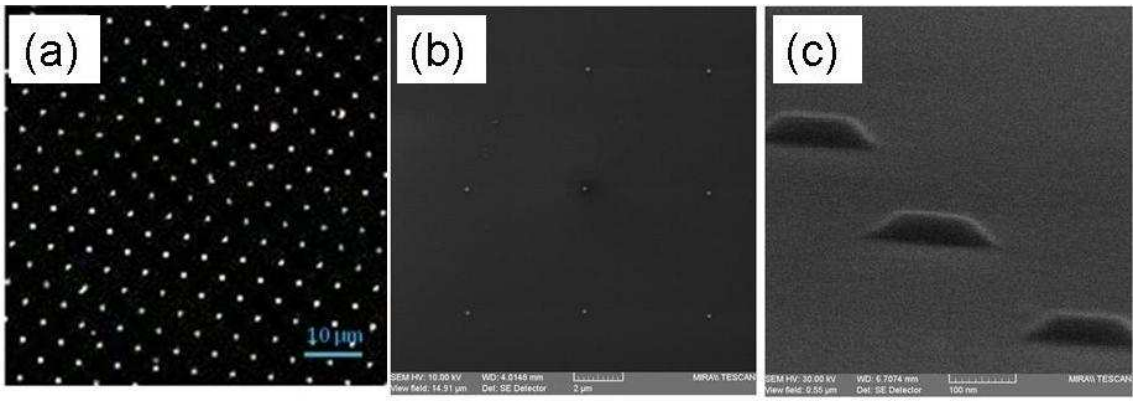

Figure 3.8. Optical and scanning electron microscope (SEM) images of the nanostructures. (a) Dark field optical imaging of the nanopillar array. (b) SEM imaging of the array. (c) A SEM image taken at an angle shows the height and uniformity of the nanostructures.

Additional topographical information was obtained using atomic force microscope imaging of the substrate, show in Fig. 3.9(a). The line profiles of Fig. 3.9(b) demonstrate

the uniformity of the $CoFe_2O_4$ dots on SiO_2. All dots have nearly identical widths and are roughly 60 nm in height.

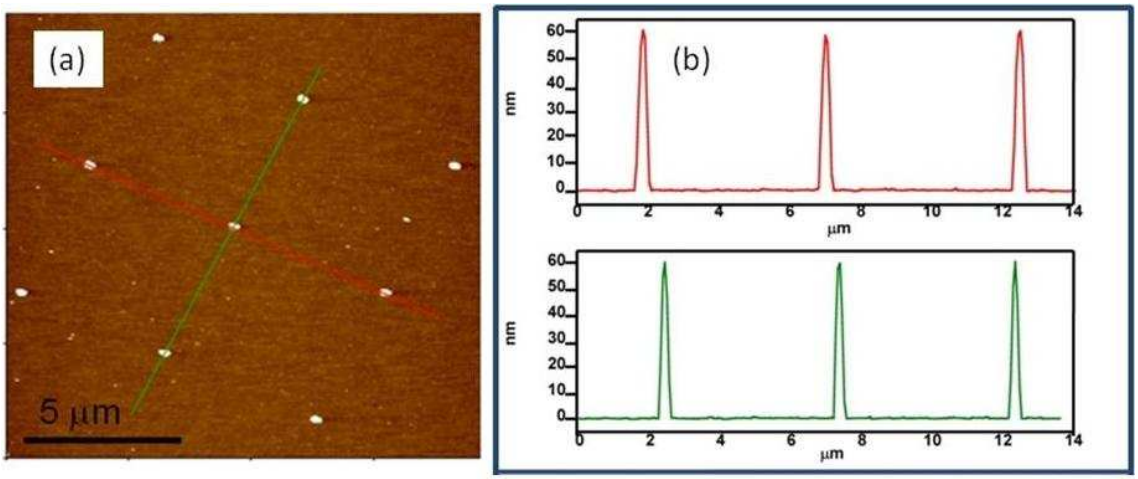

Figure 3.9. (a) Atomic force microscopy of the array of $CoFe_2O_4$ nanopillars on oxidized silicon. (b) The line profile reveals that the structures are of uniform height (60 nm) and width.

By using a combination of atomic force microscopy (AFM) and magnetic force microscopy (MFM), the magnetic and topographical signals are distinguishable from one another, thereby allowing the magnetic properties of the nanostructures to be deduced. Figure 3.10(a) shows a topographical image of a single elliptical dot. The major axis of the ellipse is approximately 300 nm and the minor axis is approximately 200 nm. Figure 3.10(b) shows an image of the same dot, this time captured using a magnetic tip. This MFM image of the dot is distinct from the topographical image of Fig. 3.10(a). In particular, magnetic domains, indicated by alternating bright and dark regions, can be observed in the image obtained using magnetic force microscopy, while no such domains are observed through atomic force microscopy. In the MFM image, the magnetization direction changes from the center to the circumference of the nanostructure: the dark field in the

center of the structure indicates that the field has deflected the magnetic cantilever, while the light field near the circumference indicates that at this point, the magnetic cantilever feels an attractive pull from the magnetic nanostructure. It can therefore be concluded that although dots have been fabricated that appear to exhibit ferromagnetic properties, single domain $CoFe_2O_4$ has not been achieved at this length scale.

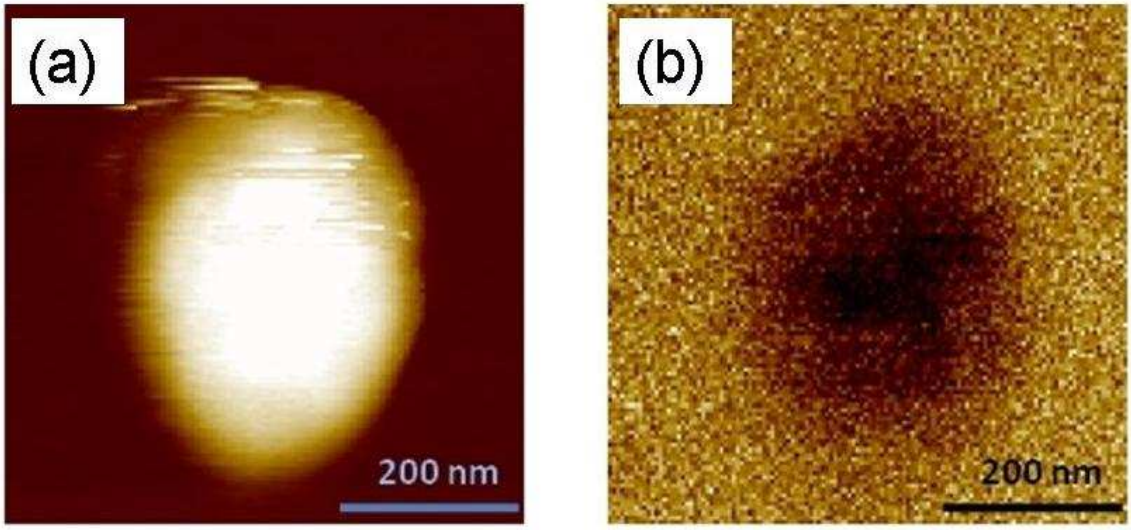

Figure 3.10. Atomic force microscopy (AFM) and magnetic force microscopy (MFM) of a single $CoFe_2O_4$ dot on oxidized silicon. (a) The AFM image shows that the structures are elliptical. (b) The MFM image reveals a magnetic domain structure that is distinct from the dot's topography and that varies from the center to the sides of the ellipse.

Ferromagnetic resonance (FMR) spectroscopy tests were performed in the EPR facility at Northwestern University to measure the dynamic magnetic properties of the nanostructures. The sample was placed in a microwave cavity and the radiation frequency was set at 9.37 GHz. An increasing magnetic field with maximal field strength of 6 kOe was applied to the material at several different rotation angles. As the magnetic field was increased, the frequency of the spin precession increased until it exactly matched the frequency of

the microwave radiation, at which point we see peak intensity in the absorption spectrum of the material. For the FMR spectra shown in Fig. 3.11, a double-peak structure is observed in the absorption spectrum, which is typical in experiments performed on bulk $CoFe_2O_4$ [**24**]. If the material is single crystalline, the magnetic field at which peak absorption occurs will change as the structures are rotated due to the shape anisotropy of the crystal. However, all spectra shown in Fig. 3.11 reach peak intensities at the same field indicated by the red arrow, roughly 3500 Oe, suggesting that there is no observable difference in axis orientation and providing further evidence that the structures are polycrystalline with multiple magnetic domains.

3.6. $CoFe_2O_4$ nanopillars on $BiFeO_3$

$BiFeO_3$ is a ferroelectric and slightly antiferromagnetic material with perovskite lattice structure. The atomic spacing in $BiFeO_3$ is almost identical to that of $CoFe_2O_4$, and due to near lattice matching between the materials, it is expected that the nanostructure fabrication process outlined above will yield single domain $CoFe_2O_4$ nanostructures on a $BiFeO_3$ substrate. Following the procedure for $CoFe_2O_4$ on SiO_2 wafers, $CoFe_2O_4$ nanostructures were synthesized on a substrate consisting of a thin film of $BiFeO_3$ on top of $SrTiO_3$. The $BiFeO_3$ was deposited on $SrTiO_3$ using pulsed laser deposition (PLD). Prior to nanostructure fabrication, the $BiFeO_3$ film was imaged using atomic force microscopy (Fig. 3.12(a)), revealing an average surface roughness of 2 nm (Fig. 3.12(b)). Furthermore, the crystal structure of the $BiFeO_3$ can be seen in the three dimensional image of Fig. 3.12(c). Because of the similar lattice spacing of $BiFeO_3$ and $CoFe_2O_4$, $CoFe_2O_4$

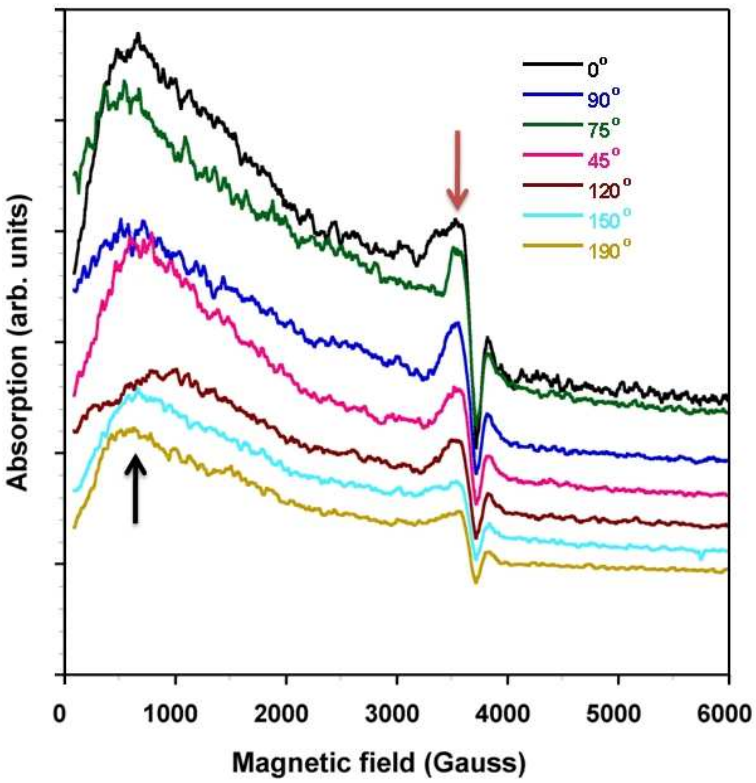

Figure 3.11. Ferromagnetic resonance spectroscopy of the nanopillar array. The double-peak structure in the absorption spectrum, indicated by the arrows, is characteristic of bulk $CoFe_2O_4$. The magnetic field of peak intensity, shown by the red arrow, does not change as the material is rotated, indicating that the nanostructures are polycrystalline.

grown on the surface of $BiFeO_3$ should yield crystal growth that mirrors the crystal structure of the $BiFeO_3$. Figure 3.12(d) shows the results of X-ray diffraction performed on the $BiFeO_3$ on $SrTiO_3$. The areas of peak intensity have Miller indices characteristic of $BiFeO_3$ and $SrTiO_3$, indicating that the materials on this wafer have the same phase as $BiFeO_3$ and $SrTiO_3$.

The previously-outlined procedure was followed to fabricate $CoFe_2O_4$ nanopillars on epitaxial $BiFeO_3$. The topography of the resulting nanostructures was distinctly different from the case of $CoFe_2O_4$ deposited on SiO_2 wafers. Figure 3.13(a) shows an array of

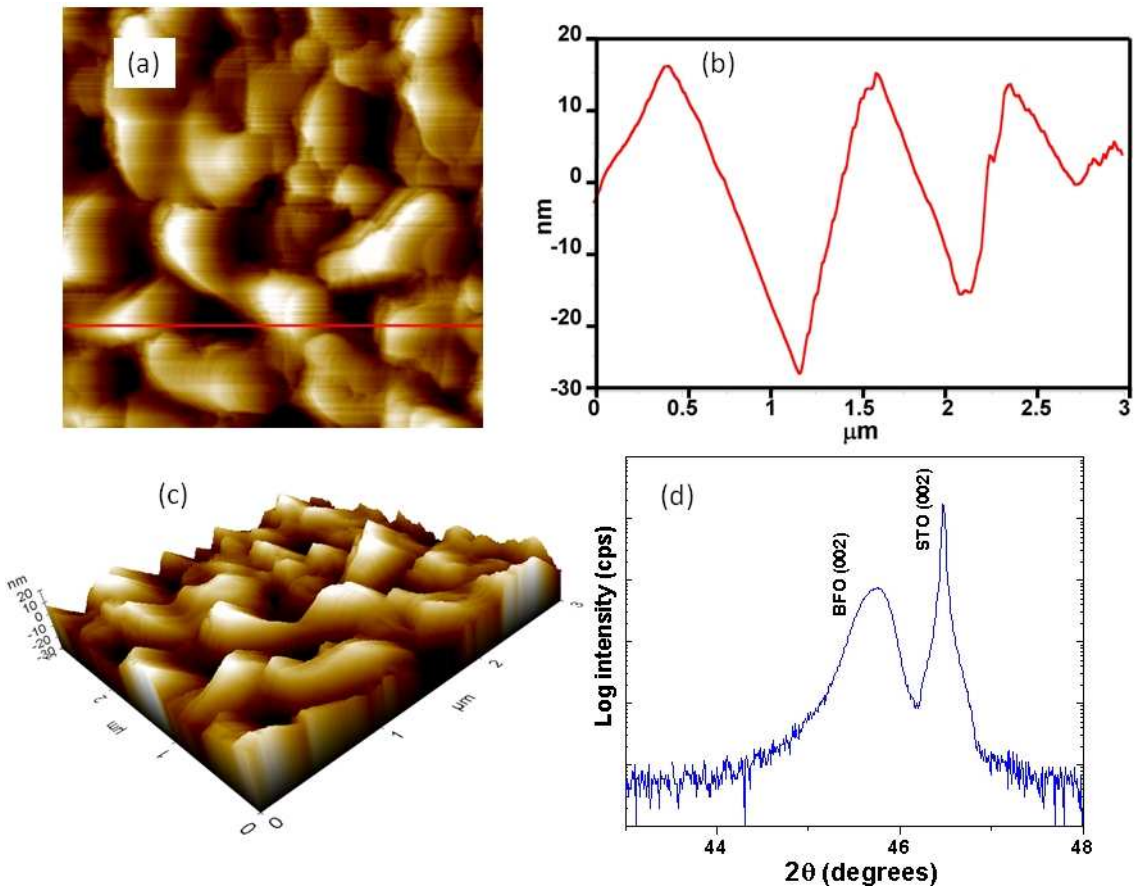

Figure 3.12. Analysis of the $BiFeO_3/SrTiO_3$ substrate. (a) Atomic force microscopy (AFM) of the $BiFeO_3$ thin film. (b) The corresponding line profile reveals a surface roughness of 2 nm. (c) A three dimensional representation of the AFM image depicts the crystalline structure of the $BiFeO_3$ film. (d) X-ray diffraction (XRD) performed on the wafer shows peak intensities corresponding to the Miller indices of $BiFeO_3$ and $SrTiO_3$.

$CoFe_2O_4$ dots grown on $BiFeO_3$ and Fig. 3.13(b) provides the corresponding line profiles. The pillars have sharp peaks, and their heights range from roughly 150 to 300 nm. When SiO_2 wafers were used as the substrate, the resulting nanopillars had equal heights of 60 nm and were flat at the top. Figure 3.13(c) shows a three dimensional representation of a single $CoFe_2O_4$ dot obtained by atomic force microscopy and provides further confirmation

of the unusual shapes of the nanopillars. The structures may arise from the fact that the $CoFe_2O_4$ layer follows the rough surface topography of the $BiFeO_3$. Additionally, overgrowth of the nanopillars beyond the PMMA thickness (∼100 nm) could be a sign of facet growth, suggesting that the $CoFe_2O_4$ may be single-crystalline.

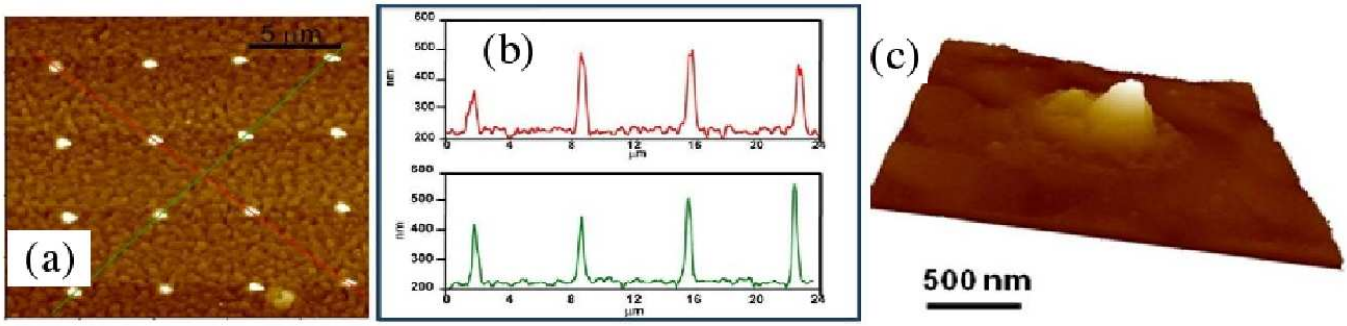

Figure 3.13. Atomic force microscopy (AFM) analysis of the $CoFe_3O_4$ nanopillars grown on $BiFeO_3$. (a) AFM imaging shows the topography of the array of the nanostructures. (b) The corresponding line profile reveals that the nanopillars have sharp peaks and heights ranging from 150 nm to 300 nm. (c) A three dimensional representation of a single $CoFe_3O_4$ dot shows its irregular structure.

CHAPTER 4

Discussion

In this paper, steps towards the realization of the composite $BiFeO_3/CoFe_2O_4$ have been presented. Through a combination of electron beam lithography and a chemical sol-gel technique, arrays of $CoFe_2O_4$ nanopillars were fabricated on both oxidized silicon and epitaxial thin films of ferroelectric $BiFeO_3$.

The topographical features of the nanopillars varied greatly between the two substrates. The structures grown on oxidized silicon were uniformly 60 nm in height, which is less than the estimated thickness of the PMMA mask ($\sim$100 nm) used for electron beam lithography. They were flat on top and showed no evidence of single crystallinity. The nanopillars grown on $BiFeO_3$, however, were of varying heights ranging from 150 nm to 300 nm, which are up to five times the heights of the pillars seen on oxidized silicon. The overgrown structures also show signatures of faceted growth. This suggests that the $CoFe_2O_4$ nanostructures grown on $BiFeO_3$ may have grown in the form of single crystals. Additionally, the nanopillars had irregular shapes and sharp triangular peaks. The shape of the pillars largely resembled the surface topography of the $BiFeO_3$, suggesting that the fabrication process led to the formation of $CoFe_2O_4$ with a structure that followed the topography of $BiFeO_3$.

While SQUID magnetometry confirmed the ferromagnetic state of the nanostructures, ferromagnetic resonance spectroscopy performed on the $CoFe_2O_4$ nanopillars on oxidized silicon indicated that polycrystalline pillars with multiple magnetic domains had been

formed. The presence of multiple magnetic domains indicates that, even at this small length scale, magnetocrystalline anisotropy dominated over shape anisotropy. In other words, orientation of the magnetic dipoles was not restricted by the shape of the nanostructures, preventing the formation of single-domain $CoFe_2O_4$.

In order to see a pronounced magnetoelectric effect, the magnetostrictive material should be both single-crystalline and single-domain. Single-crystalline $CoFe_2O_4$ would allow for clamping between the ferroelectric and ferrimagnetic layers, creating a large magnetoelectric coupling coefficient. For single-domain $CoFe_2O_4$, the material's magnetization direction could be uniformly controlled by an external electric field. Therefore, future experimentation will aim to produce single-domain and single-crystalline pillars of magnetostrictive materials such as $CoFe_2O_4$ on ferroelectrics such as $BiFeO_3$. One promising option is to explore other possible composites that can be fabricated using the combined electron beam lithography and sol-gel deposition route used for $BiFeO_3/CoFe_2O_4$. Currently, sol-gel synthesis of ferroelectric $BiFeO_3$, ferroelectric $Pb(Zr_{0.52}Ti_{0.48})O_3$ (or PZT), and magnetostrictive $La_{0.8}Sr_{0.2}MnO_3$ is being explored. By using the sol-gel method, there is great potential for improved multiferroic composites of these materials. For example, fabrication of $BiFeO_3$ by sol-gel may produce a smoother surface that would allow for uniform crystal growth of the $CoFe_2O_4$ nanopillars on the substrate. $CoFe_2O_4$/PZT composites may also exhibit a pronounced magnetoelectric effect due to similar lattice spacing of the materials [**25**].

CHAPTER 5

Conclusion

In summary, progress towards the fabrication of a multiferroic material and its characterization has been accomplished. Nanopillars of $CoFe_2O_4$ have been developed on oxidized silicon and on ferroelectric $BiFeO_3$, and the novel topographical and magnetic properties of these materials have been confirmed through a series of experimental techniques. Further research in this area is now necessary in order to achieve nanostructures that are single-crystalline, which would allow for effective clamping, and single-domain, which would enable greater control over the magnetization, consequently yielding an enhanced magnetoelectric effect. The realization of such a composite promises to give rise to efficient magnetic switching, which would bear great implications for electronic and technological applications.

Acknowledgements

There are many researchers without whom I would not have been able to achieve the same level of thoroughness and rigor in this experiment. I am especially grateful for the contributions of Erik Offerman, who patterned numerous samples using electron beam lithography and who performed SEM imaging of the nanostructures, Professor Dmitriy Dikin, who provided an SEM image of the $CoFe_2O_4$ film on SiO_2, Chad Folkman of the University of Wisconsin - Madison, who fabricated thin films of $BiFeO_3$ on $SrTiO_3$ and performed XRD analysis of the films, and Dr. Goutam Sheet, who carried out ferromagnetic resonance spectroscopy, SQUID magnetometry, and X-ray diffraction analysis of the samples, and who aided me with atomic and magnetic force microscopy.

Finally, thank you to all who have allowed for my research to be constantly stimulating and challenging. Thank you for the numerous discussions and lessons, not only in condensed matter physics, but also in a broad range of other physics and science topics. In particular, thank you to Professor Venkat Chandrasekhar, Dr. Goutam Sheet, and Manan Mehta.

References

[1] J. Ryu, S. Priya, K. Uchino, and H.J. Kim, Phys. J. Electroceramics **8**, 112 (2002).

[2] M. Vopsaroiu, J. Blackburn, and M.G. Cain, J. Phys. D: Appl. Phys. **40**, 5027 (2007).

[3] J.P. Rivera, Ferroelectrics **161**, 165 (1994).

[4] B.I. AlShin and D.N. Astrov, So. Phys. – JETP **17**, 809 (1963).

[5] G.T. Rado, Phys. Rev. Lett. **13**, 335 (1964).

[6] T. Watanabe and K. Kohn, Phase Trans. **15**, 57 (1989).

[7] M.J. Fiebig, Phys. D: App. Phys. **38**, R123 (2005).

[8] P. Calvani, M. Capizzi, F. Donato, S. Lupi, P. Maselli, and D. Peschiaroli, Phys. Rev. B **47**, 8917 (1993).

[9] S. Donthu, Z. Pan, B. Myers, G. Shekhawat, N. Wu, and V.P. Dravid, Nano Lett., **5**(9), 1710 (2005).

[10] Z. Pan, S. Donthu, N. Wu, S. Li, and V.P. Dravid, Small **2**(2), 274 (2006).

[11] H.W. Jang, D. Ortiz, S.H. Baek, C.M. Folkman, R.R. Das, P. Shafer, Y. Chen, C.T. Nelson, X. Pan, R. Ramesh, and C.B. Eom, Adv. Mat. **21**(7), 817 (2009).

[12] W.C. Rntgen, Ann. Phys. **35**, 264 (1888).

[13] H.A. Wilson, Phil. Trans. R. Soc. A **204**, 129 (1905).

[14] G.T. Rado, "Present Status of the Theory of Magnetoelectric Effects." *Symposium on Magnetoelectric Interaction Phenomena in Crystals*. A.J. Freeman and H. Schmid (ed.) (Gordon and Breach, Science Publishers Ltd., London, 1997) 3.

[15] C.A. Kittel, *Introduction to Solid State Physics, 7th ed.* (John Wiley & Sons, Inc., New York, 1996).

[16] A. Preumont, *Mechatronics: Dynamics of Electromechanical and Piezoelectric Systems, 2nd ed.* (Springer, Netherlands, 2006) 98.

[17] S.W. Tsai and H.T. Hahn, *Introduction to Composite Materials* (Technomic Publishing Company, Inc., Lancaster, PA , 1980).

[18] C.B. Carter and G.M. Norton, *Ceramic Materials: Science and Engineering* (Springer, New York, 2007) 607.

[19] G.P. McKnight, Magnetostrictive Materials Background. UCLA Active Materials Lab. <http://aml.seas.ucla.edu/home.htm>.

[20] Y.K. Fetisov, Bulletin of the Russian Academy of Sciences: Physics **71**(11), 1626 (2007).

[21] J. Lee, J.Y. Park, Y. Oh., and C.S. Kim, J. App. Phys. **84**(5), 2801 (1998).

[22] Z. G. Suna and H. Akinaga, Appl. Phys. Lett. **86**, 181904 (2005).

[23] C. Spezzani, M. Fabrizioli, P. Candeloro, E.D. Fabrizio, G. Panaccione, and M. Sacchi, Phys. Rev. B **69**, 224412 (2004).

[24] P.E. Tannenwald, Phys. Rev. **99**(2), 463 (1955).

[25] Z.Y. Li, J.G. Wan, X.W. Wang, Y. Wang, J.S. Zhu, G.H. Wang, and J.-M. Liu, Integrated Ferroelectrics **87**, 33 (2007).

[26] U. Schoop, M. Schonecke, S. Thienhaus, F. Herbstritt, J. Klein, L. Alff, and R. Fross, Physica C **350**, 237-243 (2001).